

# SCIENTIFIC DATA

OPEN

## An ATAC-seq atlas of chromatin accessibility in mouse tissues

DATA DESCRIPTOR

ChuanYu Liu<sup>1,2,3</sup>, Mingyue Wang<sup>1,2,3</sup>, Xiaoyu Wei<sup>1,2,3</sup>, Liang Wu<sup>1,2,3</sup>, Jiangshan Xu<sup>1,2,3</sup>, Xi Dai<sup>1,2,3</sup>, Jun Xia<sup>1,2,4</sup>, Mengnan Cheng<sup>1,2,3</sup>, Yue Yuan<sup>1,2,3</sup>, Pengfan Zhang<sup>1,2,3</sup>, Jiguang Li<sup>2,4</sup>, Taiqing Feng<sup>2,4</sup>, Ao Chen<sup>2,3</sup>, Wenwei Zhang<sup>2,3</sup>, Fang Chen<sup>2,3,4,5</sup>, Zhouchun Shang<sup>2,3</sup>, Xiuqing Zhang<sup>1,2,3</sup>, Brock A. Peters<sup>2,3,4,6</sup> & Longqi Liu<sup>2,3</sup>

Received: 29 November 2018

Accepted: 10 April 2019

Published online: 20 May 2019

The Assay for Transposase-Accessible Chromatin using sequencing (ATAC-seq) is a fundamental epigenomics approach and has been widely used in profiling the chromatin accessibility dynamics in multiple species. A comprehensive reference of ATAC-seq datasets for mammalian tissues is important for the understanding of regulatory specificity and developmental abnormality caused by genetic or environmental alterations. Here, we report an adult mouse ATAC-seq atlas by producing a total of 66 ATAC-seq profiles from 20 primary tissues of both male and female mice. The ATAC-seq read enrichment, fragment size distribution, and reproducibility between replicates demonstrated the high quality of the full dataset. We identified a total of 296,574 accessible elements, of which 26,916 showed tissue-specific accessibility. Further, we identified key transcription factors specific to distinct tissues and found that the enrichment of each motif reflects the developmental similarities across tissues. In summary, our study provides an important resource on the mouse epigenome and will be of great importance to various scientific disciplines such as development, cell reprogramming, and genetic disease.

### Background & Summary

Although most of the protein-coding genes in human and model animals such as mouse have been extensively annotated, vast regions of the genome are noncoding sequences (e.g., roughly 98% of the human genome) and still poorly understood<sup>1,2</sup>. During the last decade, the development of next-generation sequencing (NGS) based epigenomics techniques (e.g., ChIP-seq and DNase-seq) have significantly facilitated the identification of functional genomic regions<sup>3</sup>. For example, by comparing the histone modifications and transcription factor (TF) binding patterns throughout the mouse genome in a wide spectrum of tissues and cell types, Yue *et al.*<sup>4,5</sup> have made significant progress towards a comprehensive catalog of potential functional elements in the mouse genome. So far, the international human epigenome consortium (IHEC), including ENCODE and the NIH Roadmap epigenomics projects, have profiled thousands of epigenomes including DNA methylation, genome-wide binding of TFs, histone modifications, and chromatin accessibility. This has resulted in the discovery of over 5 million *cis*-regulatory elements (CREs) in the human genome<sup>6–8</sup>. These data resources have created an important baseline for further study of diverse biological processes, such as development, cell reprogramming, and human disease<sup>9–13</sup>.

The accessibility of CREs, which is important for switching on and off gene expression<sup>14</sup>, is strongly associated with transcriptional activity. To date, detection of DNase I hypersensitive sites (DHSs) within chromatin by DNase-seq has been extensively used to map accessible genomic regions in diverse organisms including the laboratory mouse<sup>5</sup>. In 2013, Buenrostro *et al.*<sup>15</sup> reported an alternative approach, termed ATAC-seq, for fast and sensitive profiling of chromatin accessibility by direct transposition of native chromatin within the nucleus. This method, in comparison to DNase-seq, requires a significantly lower input of cells (only 500–50,000) and a shorter period to process samples<sup>16</sup>. Moreover, ATAC-seq has been applied to single cells through various methods<sup>17–20</sup>,

<sup>1</sup>BGI Education Center, University of Chinese Academy of Sciences, Shenzhen, 518083, China. <sup>2</sup>BGI-Shenzhen, Shenzhen, 518083, China. <sup>3</sup>China National GeneBank, BGI-Shenzhen, Shenzhen, 518120, China. <sup>4</sup>MGI, BGI-Shenzhen, Shenzhen, 518083, China. <sup>5</sup>Laboratory of Genomics and Molecular Biomedicine, Department of Biology, University of Copenhagen, Copenhagen, 2100, Denmark. <sup>6</sup>Advanced Genomics Technology Lab, Complete Genomics Inc., 2904 Orchard Parkway, San Jose, California, 95134, USA. These authors contributed equally: ChuanYu Liu, Mingyue Wang and Xiaoyu Wei. Correspondence and requests for materials should be addressed to B.A.P. (email: [bpeters@completegenomics.com](mailto:bpeters@completegenomics.com)) or L.L. (email: [liulongqi@genomics.cn](mailto:liulongqi@genomics.cn))

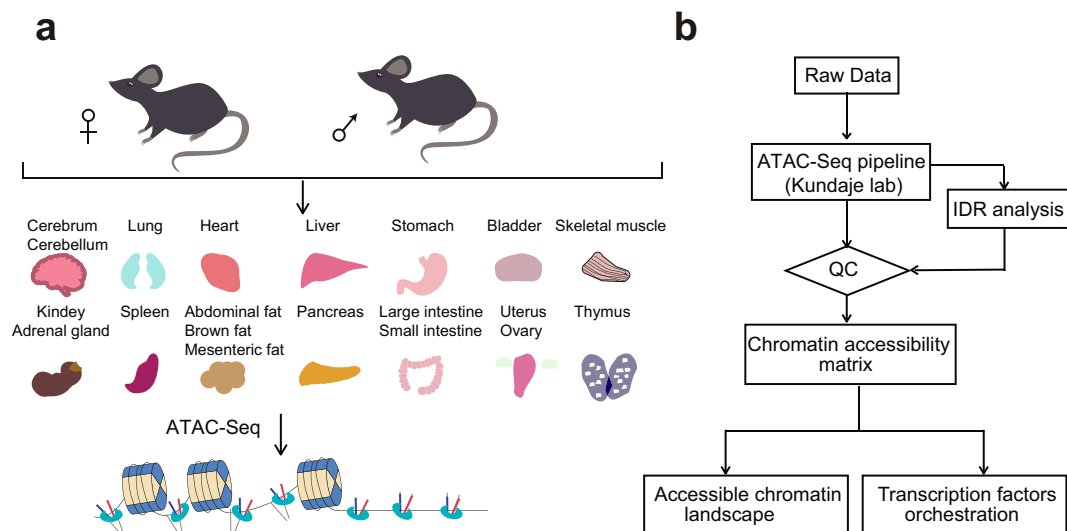


**Fig. 1** Overview of the experimental and data analysis workflow. **(a)** 20 different tissues from adult mice were collected for ATAC-seq profiling. **(b)** The analysis workflow for ATAC-seq profiles.

enabling the investigation of regulatory heterogeneity within complex tissues. As such, ATAC-seq has demonstrated great potential to be a leading method in assaying accessible chromatin genome-wide.

The sequence preference of both DNase I and Tn5 enzymes produced distinct but inevitable biases in DNase-seq and ATAC-seq<sup>21</sup>, making it impractical to directly compare datasets generated from the two methods. Therefore, although the DNase-seq atlas of adult mouse tissues has been published<sup>5</sup>, a baseline of chromatin accessible regions generated from ATAC-seq is still important for ATAC-seq based studies. Here, we applied Omni-ATAC-seq<sup>22</sup>, an approach that enables profiling of accessible chromatin from frozen tissues, to the generation of 66 chromatin accessibility datasets from 20 different tissues derived from both adult male and female C57BL/6J mice (Fig. 1a). Systematic analysis of the dataset identified a total of 296,574 accessible elements, of which 26,916 showed highly tissue-specific patterns. We further predicted TFs specific to distinct tissues and importantly, many of these have been validated by previous studies<sup>23–27</sup>. In this study, we provide a valuable resource, which can be used to elucidate transcriptional regulation and may further help understand diseases caused by regulatory dysfunction.

## Methods

**Sample collection.** All relevant procedures involving animals were approved by the Institutional Review Board on Ethics Committee of BGI (Permit No. BGI-R085-1). C57BL/6J male and female mice were purchased from Beijing Vital River Laboratory Animal Technology Co., Ltd (Beijing, China). 8-week old mice were used for this study. Mice were housed under standard conditions of a specific pathogen-free, temperature-controlled environment with a 12-h day/night cycle<sup>28</sup>. The mice were sacrificed by cervical dislocation. Whole organs were extracted and cut into 2–3 pieces, respectively (50–200 mg/piece). Each sample was then quickly frozen in liquid nitrogen and stored at  $-80^{\circ}\text{C}$  until nuclei extraction was performed. In this study, we used 20 different organs or tissues, including adrenal gland, bladder, brain (cerebrum and cerebellum), fat (abdominal, brown and mesenteric), heart, intestine (large and small), kidney, liver, lung, ovary, pancreas, skeletal muscle, spleen, stomach, thymus, and uterus (as listed in Table 1).

**Library construction and sequencing.** Tissues were homogenized in a 2 ml Dounce homogenizer (with a loose and then tight pestle) with 10–20 strokes in 2 ml of 1X homogenization buffer on ice<sup>22</sup>. 400  $\mu\text{l}$  of this nuclei suspension was transferred to a round-bottom 2 ml Lo-Bind Eppendorf tube for density gradient centrifugation following the protocol by Corces *et al.*<sup>22</sup>. After centrifugation, the nuclei band (about 200  $\mu\text{l}$ ) was collected, stained with DAPI, and nuclei were counted. Approximately 20,000–100,000 nuclei were transferred into a fresh tube and diluted in 1 ml ATAC-RSB + 0.1% Tween-20 (Sigma-Aldrich, Darmstadt, Germany). Nuclei were centrifuged and the supernatant was carefully aspirated. Nuclei were treated in 50  $\mu\text{l}$  transposition reaction mixture containing 10 mM TAPS-NaOH (pH 8.5), 5 mM  $\text{MgCl}_2$ , 10% DMF, 2.5  $\mu\text{l}$  of in-house Tn5 transposase (0.8 U/ $\mu\text{l}$ ), 0.01% digitonin (Sigma-Aldrich, Darmstadt, Germany), 0.1% Tween-20, 31.5  $\mu\text{l}$  of PBS, and 5  $\mu\text{l}$  of nuclease-free water for 30 mins at  $37^{\circ}\text{C}$ . Afterward, the DNA was purified with MinElute Purification Kit (Qiagen, Venlo, Netherlands) and amplified with primers containing barcodes, as previously described<sup>22,29</sup>.

All libraries were adapted for sequencing on the BGISEQ-500 platform<sup>30</sup>. In brief, the DNA concentration was determined by Qubit 3.0 (ThermoFisher, Waltham, MA). Pooled samples were used to make single-strand DNA circles (ssDNA circles). DNA nanoballs (DNBs) were generated from the ssDNA circles by rolling circle replication as previously described<sup>30</sup>. The DNBs were loaded onto patterned nano-arrays and sequenced on the BGISEQ-500 sequencing platform with paired end 50 base reads.

Sample ID	Strain	Serial	Gender	Tissue	Replicate
ATAC-1	C57BL/6J	1	Female	Adrenal gland	1
ATAC-2	C57BL/6J	1	Female	Adrenal gland	2
ATAC-3	C57BL/6J	1	Female	Cerebrum	1
ATAC-4	C57BL/6J	1	Female	Cerebrum	2
ATAC-5	C57BL/6J	1	Female	Cerebellum	1
ATAC-5	C57BL/6J	1	Female	Cerebellum	2
ATAC-7	C57BL/6J	1	Female	Abdominal fat	1
ATAC-8	C57BL/6J	1	Female	Abdominal fat	2
ATAC-9	C57BL/6J	1	Female	Brown fat	1
ATAC-10	C57BL/6J	1	Female	Brown fat	2
ATAC-11	C57BL/6J	1	Female	Mesenteric fat	1
ATAC-12	C57BL/6J	1	Female	Mesenteric fat	2
ATAC-13	C57BL/6J	1	Female	Heart	1
ATAC-14	C57BL/6J	1	Female	Heart	2
ATAC-15	C57BL/6J	1	Female	Kidney	1
ATAC-16	C57BL/6J	1	Female	Kidney	2
ATAC-17	C57BL/6J	1	Female	Liver	1
ATAC-18	C57BL/6J	1	Female	Liver	2
ATAC-19	C57BL/6J	1	Female	Lung	1
ATAC-20	C57BL/6J	1	Female	Lung	2
ATAC-21	C57BL/6J	1	Female	Ovary	1
ATAC-22	C57BL/6J	1	Female	Ovary	2
ATAC-23	C57BL/6J	1	Female	Pancreas	1
ATAC-24	C57BL/6J	1	Female	Pancreas	2
ATAC-25	C57BL/6J	1	Female	Skeletal muscle	1
ATAC-26	C57BL/6J	1	Female	Skeletal muscle	2
ATAC-27	C57BL/6J	1	Female	Spleen	1
ATAC-28	C57BL/6J	1	Female	Spleen	2
ATAC-29	C57BL/6J	1	Female	Thymus	1
ATAC-30	C57BL/6J	1	Female	Thymus	2
ATAC-31	C57BL/6J	1	Female	Uterus	1
ATAC-32	C57BL/6J	1	Female	Uterus	2
ATAC-33	C57BL/6J	2	Male	Adrenal gland	1
ATAC-34	C57BL/6J	2	Male	Adrenal gland	2
ATAC-35	C57BL/6J	2	Male	Bladder	1
ATAC-36	C57BL/6J	2	Male	Bladder	2
ATAC-37	C57BL/6J	2	Male	Cerebrum	1
ATAC-38	C57BL/6J	2	Male	Cerebrum	2
ATAC-39	C57BL/6J	2	Male	Cerebellum	1
ATAC-40	C57BL/6J	2	Male	Cerebellum	2
ATAC-41	C57BL/6J	2	Male	Brown fat	1
ATAC-42	C57BL/6J	2	Male	Brown fat	2
ATAC-43	C57BL/6J	2	Male	Mesenteric fat	1
ATAC-44	C57BL/6J	2	Male	Mesenteric fat	2
ATAC-45	C57BL/6J	2	Male	Heart	1
ATAC-46	C57BL/6J	2	Male	Heart	2
ATAC-47	C57BL/6J	2	Male	Large intestine	1
ATAC-48	C57BL/6J	2	Male	Large intestine	2
ATAC-49	C57BL/6J	2	Male	Small intestine	1
ATAC-50	C57BL/6J	2	Male	Small intestine	2
ATAC-51	C57BL/6J	2	Male	Kidney	1
ATAC-52	C57BL/6J	2	Male	Kidney	2
ATAC-53	C57BL/6J	2	Male	Liver	1
ATAC-54	C57BL/6J	2	Male	Liver	2
ATAC-55	C57BL/6J	2	Male	Lung	1
ATAC-56	C57BL/6J	2	Male	Lung	2
ATAC-57	C57BL/6J	2	Male	Pancreas	1
ATAC-58	C57BL/6J	2	Male	Pancreas	2
ATAC-59	C57BL/6J	2	Male	Skeletal muscle	1
ATAC-60	C57BL/6J	2	Male	Skeletal muscle	2
ATAC-61	C57BL/6J	2	Male	Spleen	1
ATAC-62	C57BL/6J	2	Male	Spleen	2
ATAC-63	C57BL/6J	2	Male	Stomach	1
ATAC-64	C57BL/6J	2	Male	Stomach	2
ATAC-65	C57BL/6J	2	Male	Thymus	1
ATAC-66	C57BL/6J	2	Male	Thymus	2

**Table 1.** Tissue and corresponding mouse and sample IDs.

Sample ID	Total Reads	Mapped Reads*	chrM Reads	Usable Reads*	Percentage of Usable Reads	TSS Enrichment	IDR Peaks
ATAC-1	98,303,382	96,954,685	23,288,521	16,098,792	16.38	17.21	23,296
ATAC-2	148,416,230	146,416,001	25,259,955	24,542,678	16.54	17.83	23,296
ATAC-3	150,254,776	148,205,698	1,773,531	116,676,430	77.65	18.35	93,546
ATAC-4	132,170,414	130,467,930	1,749,710	108,546,212	82.13	19.17	93,546
ATAC-5	44,251,998	43,732,156	254,745	35,315,756	79.81	13.90	32,337
ATAC-5	180,555,698	178,313,881	2,085,323	136,439,604	75.57	14.51	32,337
ATAC-7	170,643,536	166,598,249	1,204,915	61,090,112	35.80	13.03	28,827
ATAC-8	165,896,236	135,431,464	1,175,420	61,493,964	37.07	12.63	28,827
ATAC-9	134,023,704	129,656,384	14,098,291	49,198,612	36.71	16.75	66,620
ATAC-10	160,942,400	156,016,214	13,541,729	59,910,266	37.22	16.71	66,620
ATAC-11	157,502,400	154,297,472	1,228,888	93,224,318	59.19	8.10	34,851
ATAC-12	162,615,494	159,625,229	1,252,759	103,453,218	63.62	7.44	34,851
ATAC-13	238,728,090	229,371,653	14,280,715	116,609,704	48.85	7.82	38,875
ATAC-14	268,182,264	259,270,286	18,497,755	132,829,548	49.53	7.11	38,875
ATAC-15	90,269,090	88,799,485	1,190,916	67,126,022	74.36	13.93	57,348
ATAC-16	108,421,198	106,752,478	1,697,128	77,533,954	71.51	13.54	57,348
ATAC-17	137,779,770	135,420,287	647,765	103,420,718	75.06	7.56	49,444
ATAC-18	138,236,344	135,957,141	603,586	103,420,718	74.81	7.24	49,444
ATAC-19	181,243,756	178,738,131	1,480,812	135,096,206	74.54	12.98	74,408
ATAC-20	123,570,800	121,933,521	1,153,158	96,071,108	77.75	13.55	74,408
ATAC-21	110,371,234	109,170,446	3,960,686	63,119,950	57.19	13.61	22,300
ATAC-22	39,326,846	38,875,707	1,497,720	24,585,734	62.52	17.13	22,300
ATAC-23	35,838,048	34,832,716	153,844	25,314,950	70.64	12.88	37,012
ATAC-24	107,196,410	104,421,905	523,370	76,018,760	70.92	12.55	37,012
ATAC-25	133,254,164	131,716,403	2,973,082	63,522,884	47.67	6.39	16,386
ATAC-26	166,638,990	164,664,788	3,405,553	75,588,356	45.36	6.04	16,386
ATAC-27	94,226,804	93,372,274	697,988	58,659,642	62.25	7.55	18,659
ATAC-28	106,958,878	106,110,973	727,572	74,085,722	69.27	7.75	18,659
ATAC-29	70,619,572	69,042,929	629,068	49,965,476	70.75	11.87	35,092
ATAC-30	89,598,654	87,444,974	844,626	62,271,590	69.50	11.50	35,092
ATAC-31	66,931,470	66,424,809	200,619	50,479,508	75.42	5.71	12,249
ATAC-32	90,829,474	74,837,342	286,587	68,853,698	75.81	6.24	12,249
ATAC-33	98,233,400	94,112,150	4,507,302	23,763,636	24.19	15.52	24,953
ATAC-34	214,082,112	198,861,218	14,028,173	40,427,112	18.88	21.83	24,953
ATAC-35	84,715,186	83,692,447	5,340,505	39,154,858	46.22	9.15	21,940
ATAC-36	212,395,310	209,869,802	16,551,961	79,600,948	37.48	9.98	21,940
ATAC-37	235,561,686	191,218,996	4,553,350	155,453,764	65.99	25.43	117,909
ATAC-38	191,218,996	188,304,479	3,834,757	130,871,008	68.44	25.58	117,909
ATAC-39	53,952,860	53,152,913	981,941	41,135,886	76.24	15.42	41,280
ATAC-40	158,893,266	156,816,876	2,293,222	107,582,560	67.71	19.42	41,280
ATAC-41	173,258,824	166,021,269	19,132,852	24,004,880	13.85	17.70	43,306
ATAC-42	136,328,522	132,274,503	11,522,990	45,461,724	33.35	17.81	43,306
ATAC-43	155,269,780	151,746,361	1,090,769	100,616,020	64.80	8.65	41,494
ATAC-44	202,037,768	198,044,341	1,146,229	136,190,834	67.41	9.22	41,494
ATAC-45	157,868,844	154,946,940	21,384,649	61,621,604	39.03	8.34	31,248
ATAC-46	136,265,518	133,201,038	13,707,672	55,085,754	40.43	8.77	31,248
ATAC-47	125,102,346	123,612,014	6,647,001	78,928,576	63.09	9.93	54,282
ATAC-48	59,245,938	58,534,297	3,079,504	39,391,956	66.49	9.89	54,282
ATAC-49	119,605,280	118,172,060	549,819	83,043,494	69.43	12.31	30,671
ATAC-50	126,897,090	125,503,611	556,836	90,393,490	71.23	11.70	30,671
ATAC-51	75,598,616	74,377,104	2,570,404	54,471,070	72.05	19.32	74,760
ATAC-52	128,285,640	126,411,530	4,825,675	87,433,334	68.16	17.13	74,760
ATAC-53	206,730,874	202,279,412	2,800,887	146,461,186	70.85	13.31	78,775
ATAC-54	194,636,430	190,999,768	3,353,166	140,032,146	71.95	13.07	78,775
ATAC-55	108,547,670	107,297,270	1,127,842	78,808,372	72.60	13.78	64,002
ATAC-56	156,741,782	155,063,216	1,616,305	113,767,728	72.58	13.15	64,002
ATAC-57	91,983,866	89,773,673	819,185	65,257,644	70.94	17.81	54,658
ATAC-58	238,980,976	232,982,918	3,255,911	162,801,402	68.12	16.01	54,658
ATAC-59	117,557,552	115,960,450	1,920,255	44,835,398	38.14	6.32	14,722
ATAC-60	214,824,060	211,626,739	2,469,962	42,681,444	19.87	9.52	14,722
ATAC-61	96,385,558	95,252,958	708,544	63,986,222	66.39	11.09	21,189
ATAC-62	99,268,666	98,104,994	736,929	67,856,328	68.36	11.95	21,189
ATAC-63	146,138,130	144,325,578	1,901,264	96,815,264	66.25	10.05	34,443
ATAC-64	53,691,468	52,961,106	1,045,366	37,522,232	69.88	13.43	34,443
ATAC-65	108,290,790	106,397,126	1,095,779	78,782,088	72.75	14.54	42,037
ATAC-66	131,298,716	128,823,646	1,286,797	93,295,128	71.06	14.16	42,037

**Table 2.** ATAC-seq metadata and mapping statistics. \*Mapped reads: total number of read minus number of unaligned read; \*Usable reads: number of mapped read minus number of low mapping quality, duplicate and mitochondrial reads.

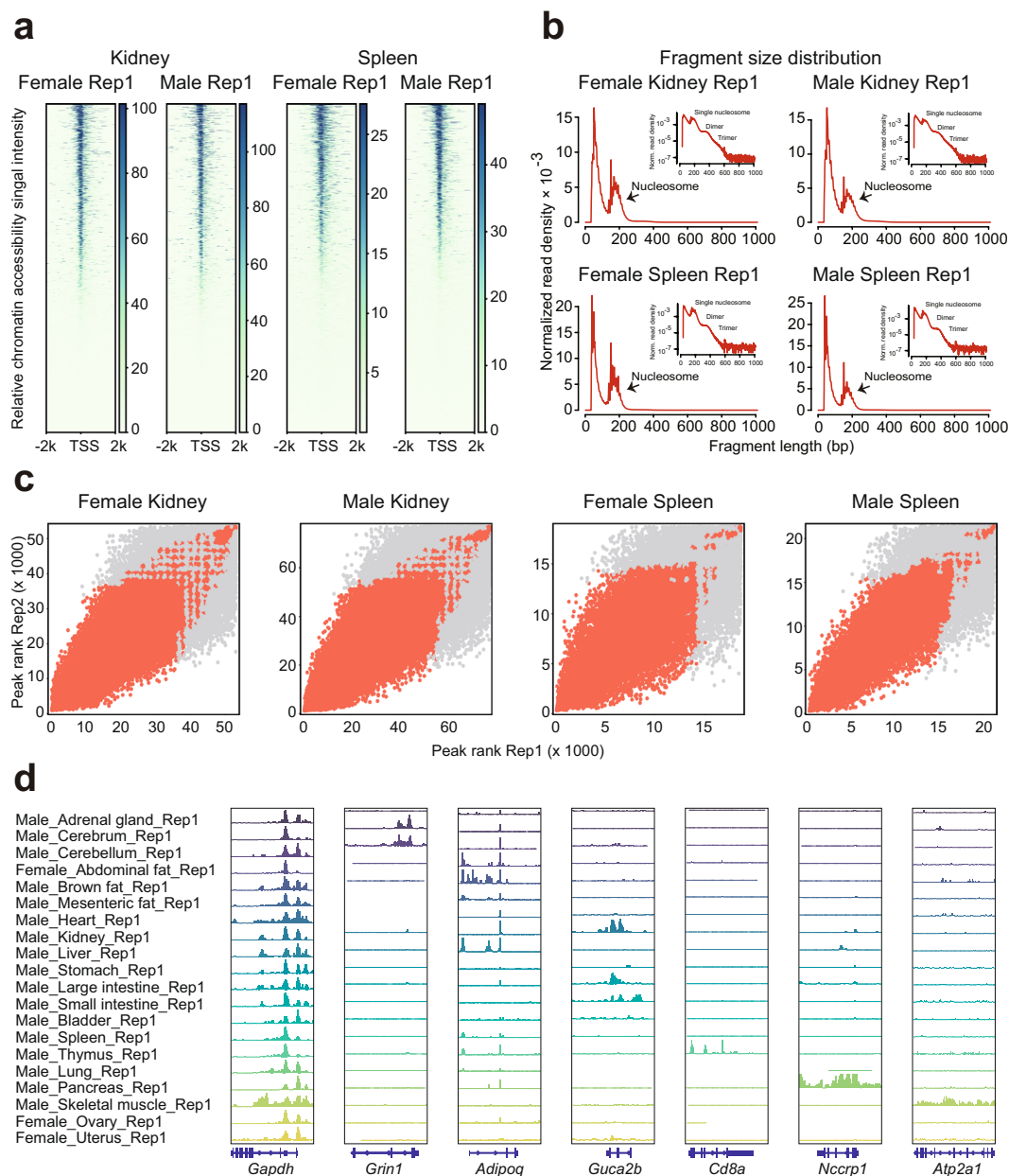


**Fig. 2** ATAC-seq data quality metrics. **(a)** The ATAC-seq signal enrichment around the transcription start sites (TSSs) for 4 representative samples (kidney or spleen of male or female mice). **(b)** The insert size distribution of ATAC-seq profiles for the same samples shown in 2a. **(c)** The irreproducible discovery rate (IDR) analyses of ATAC-seq peaks for the indicated samples. The scatter plots show points for every peak, with their location representing the rank in each replicate. **(d)** Genome browser views of ATAC-seq signal for the indicated housekeeping gene (*Gapdh*) and tissue-specific genes.

**Preprocessing of the ATAC-seq datasets.** The ATAC-seq data were processed (trimmed, aligned, filtered, and quality controlled) using the ATAC-seq pipeline from the Kundaje lab<sup>31,32</sup> (Table 2). The model-based analysis of ChIP-seq (MACS2)<sup>33</sup> version 2.1.2 was used to identify the peak regions with options -B, -q 0.01-nomodel, -f BAM, -g mm. The Irreproducible Discovery Rate (IDR) method<sup>34</sup> was used to identify reproducible peaks between two technical replicates (Fig. 1b). Only peaks reproducible between the two technical replicates were retained for downstream analyses. Peaks for all tissues were then merged together into a standard peak list. The number of raw reads mapped to each standard peak were counted using the *intersect* function of BedTools<sup>35</sup> version 2.26.0. The raw count matrix<sup>32</sup> was normalized by Reads Per Million mapped reads (RPM). Pearson correlation coefficients between technical or biological replicates across tissues were calculated based on the Log10 RPM matrix.

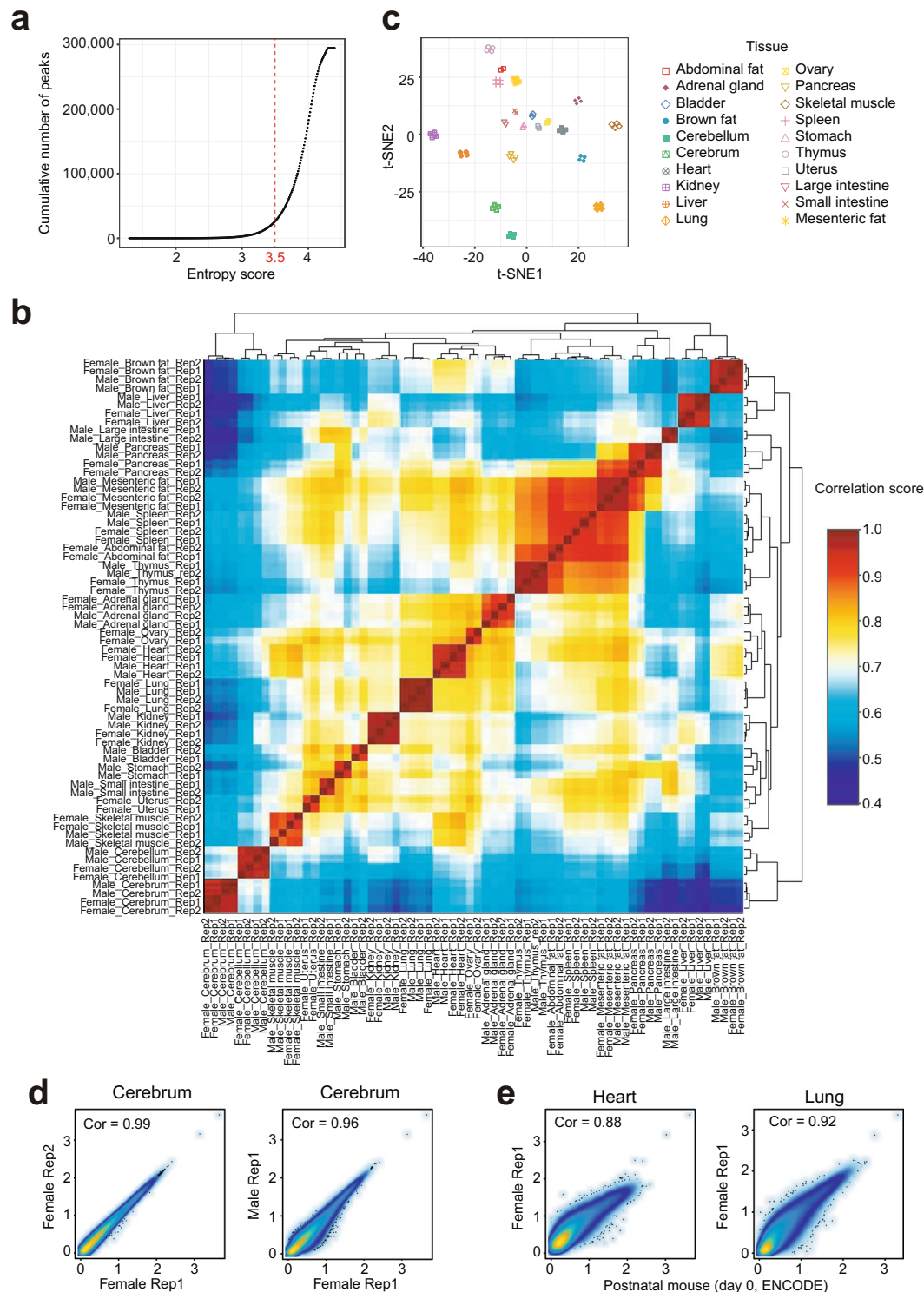


**Fig. 3** Evaluation of reproducibility across the ATAC-seq datasets. **(a)** The distribution curve of peak entropy scores. **(b)** Heatmap clustering of correlation coefficients across all 66 tissue ATAC-seq profiles. **(c)** t-SNE plot of all 66 ATAC-seq profiles based on the 26,916 tissue-specific peaks. **(d)** Scatter plots showing the Pearson correlations between technical (left) and biological (right) replicates. **(e)** Scatter plots showing the Pearson correlations between ENCODE postnatal mouse (day 0) datasets and our ATAC-seq profiles.

**Identification of tissue-specific chromatin accessible regions.** We used a strategy described previously based on the Shannon entropy to compute a tissue specificity index for each peak<sup>4,36,37</sup>. Specifically, for each peak, we defined its relative accessibility in a tissue type  $i$  as  $R_i = E_i / \sum E$ , where  $E_i$  is the RPM value for the peak in the tissue  $i$ ,  $\sum E$  is the sum of RPM values in all tissues, and  $N$  is the total number of tissues. The entropy

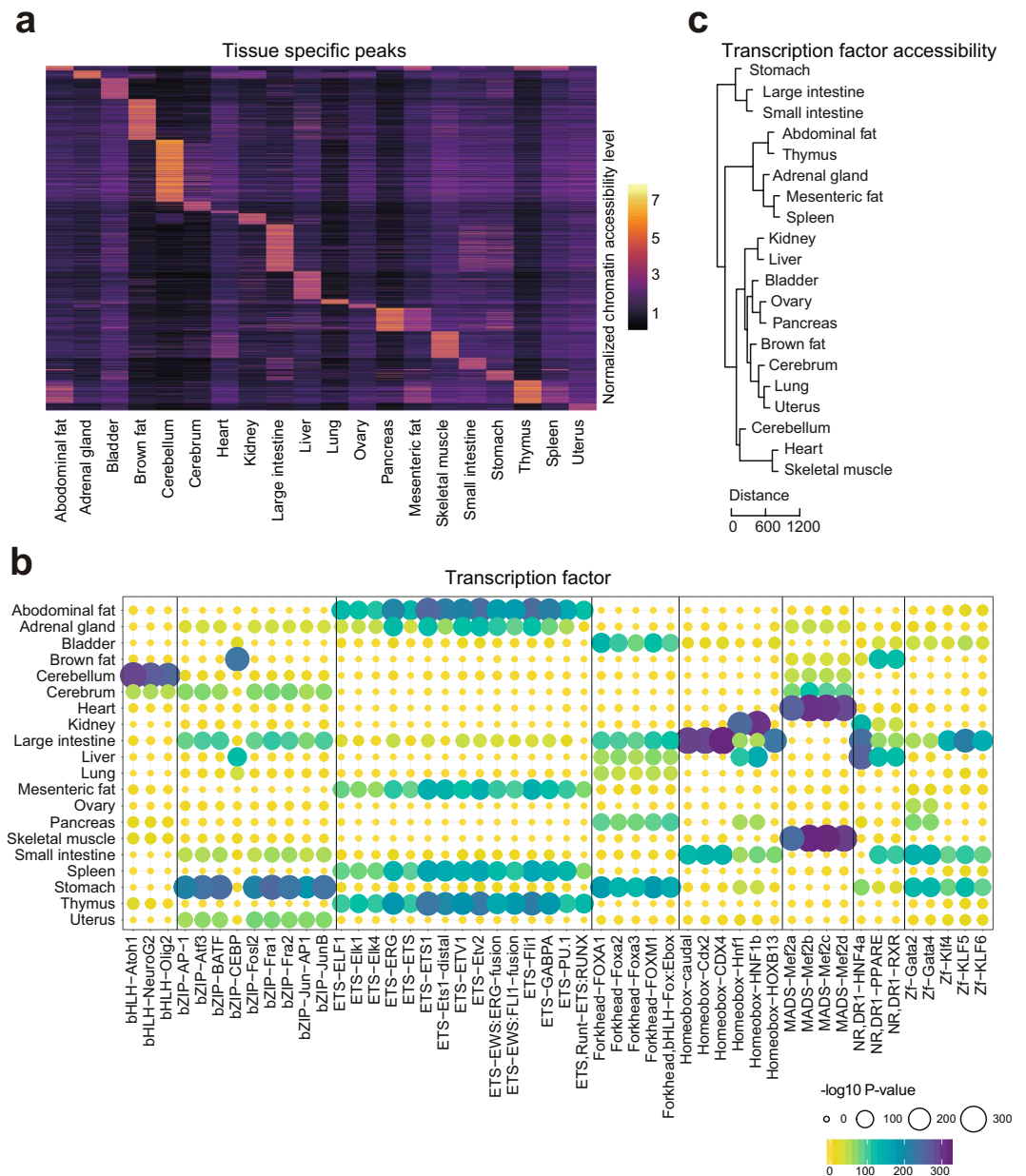


**Fig. 4** Identification of tissue-specific chromatin accessible elements and transcription factors. **(a)** Heatmap clustering showing the tissue-specific accessible elements. **(b)** Enrichment of the indicated TF motifs in each tissue. The size and color of each point represent the motif enrichment P-value ( $-\log_{10}$  P-value). **(c)** The hierarchical clustering of transcription factor enrichment scores in each tissue. Euclidian distances are shown in the legend.

score for each peak across tissues can be defined as  $H = -1 * \sum(R_i * \log_2 R_i)$  ( $1 < i < N$ ), where the value of  $H$  ranges between 0 to  $\log_2(N)$ . An entropy score close to zero indicates the accessibility of this peak is highly tissue-specific, while an entropy score close to  $\log_2(N)$  indicates that this peak is ubiquitously accessible<sup>38</sup>. Based on the distribution of entropy scores, peaks with score less than 3.5 were selected as tissue-restricted peaks.

We searched TF motifs in tissue-specific peaks using the *findMotifsGenome.pl* script of the HOMER<sup>39</sup> version 4.9.1 software with default settings. We then generated a motif enrichment matrix<sup>32</sup>, where each row represents the P-value of a motif and each column represents a tissue. The 50 motifs with the top CV values and mean values greater than 20 were displayed.

### Data Records

A complete list of the 66 tissue samples is given in Tables 1 and 2. All raw data have been submitted to the CNGB Nucleotide Sequence Archive<sup>40</sup>. The raw data have also been submitted to the NCBI Sequence Read Archive<sup>41</sup>. The ATAC-seq QC results and count matrixes have been submitted to the Figshare<sup>32</sup>.

## Technical Validation

**Data QC from the pipeline with IDR quality control.** We evaluated our ATAC-seq dataset by a series of commonly used statistics, including the number of total read, mapping rate, the proportion of duplicate read, the number of mitochondrial read, and the number of final usable read (Table 2). For each replicate, we obtained an average of 78 million reads, which was previously shown to be enough for the detection of accessible regions<sup>15,31</sup>. In agreement with published ATAC-seq profiles<sup>15</sup>, the chromatin accessibility fragments show size periodicity corresponding to integer multiples of nucleosomes<sup>32</sup> (Fig. 2b). The successful detection of accessible regions is also supported by the observation of strong enrichment of ATAC-seq reads around transcription start sites (TSSs)<sup>32</sup> (Fig. 2a,d).

To evaluate the reproducibility of accessible element discovery between replicates, we identified accessible regions in both replicates by using the MACS2<sup>33</sup> algorithm. We then applied the IDR method<sup>34</sup> to find peaks that were reproducible between replicates in each tissue type (Fig. 2c). We identified an average of 43,421 reproducible peaks (Table 2). For downstream analyses, we filtered out low-quality data where the TSS enrichment scores are less than 10.0 and the number of reproducible peaks are less than 10,000.

**Reproducibility of biological samples and comparison with published studies.** The Pearson correlation analysis was used to further examine the reproducibility of biological and technical replicates. Heatmap clustering of Pearson correlation coefficients from the comparison of 66 datasets revealed a strong correlation between replicates of the same tissue (Fig. 3b), but a lower correlation between profiles from distinct tissues. This result is also supported by t-distributed stochastic neighbor embedding (t-SNE) analysis with tissue-restricted peaks of all profiles (Fig. 3a,c). Interestingly, correlations between replicates from mice of the same gender are generally higher than those from the opposite gender. This can be seen in the cerebrum where the correlation coefficient between replicates of female mice is 0.99 (Fig. 3d), while the coefficient between male and female is slightly reduced (0.96). We also compared our data to ATAC-seq profiles of postnatal mouse (day 0) tissues downloaded from ENCODE project<sup>42,43</sup>. Importantly, we found that both heart and lung were comparable with each other (Fig. 3e). Taken together, these analyses strongly suggest that our ATAC-seq profiles can reliably detect accessible chromatin regions in the mouse genome and can be used as a basic reference ATAC-seq dataset for future studies.

**Inferring tissue-specific transcription factors.** In an effort to validate the tissue-specific TF motifs identified in our dataset, we compared them to results from previous studies. Log<sub>2</sub> RPM of the tissue-restricted peaks was shown in the heatmap (Fig. 4a). For example, we observed high enrichment of the NeuroG2 motif in cerebellum and cerebrum (Fig. 4b), in agreement with the role of NeuroG2 in controlling the temporal switch from neurogenesis to gliogenesis and regulating laminar fate transitions<sup>23</sup>. In brown fat, we found the CCAAT-enhancer-binding proteins (CEBP) motif to be highly specific (Fig. 4b). This is supported by a previous study demonstrating that CEBP can cooperate with PRDM16 to induce brown fat determination and differentiation<sup>24</sup>. In addition, other well-known tissues-specific motifs such as the liver-specific HNF family TF motifs (Hnf1, HNF1b, and HNF4a)<sup>25</sup> and heart or skeletal muscle specific Mef2 family motifs (Mef2a, Mef2b, Mef2c, Mef2d)<sup>26,27</sup> were validated in our study. To further validate whether the overall motif enrichment in each tissue can reflect tissue specificity we performed hierarchical clustering of tissues using Euclidean distance (Fig. 4c). This provided a result similar to hierarchical clustering of various mouse tissues based on RNA-seq data<sup>44</sup>. In addition, examination of tissues from the gastrointestinal (GI) tract (i.e., large intestine, small intestine, and stomach) showed tight clustering (Fig. 4c), which is likely due to their common functions such as lipid metabolism and energy homeostasis<sup>45,46</sup>. Skeletal muscle and heart tissue are found in the same branch, suggesting that patterns of chromatin accessibility in the two tissues are highly influenced by shared TF motifs such as those from the Mef2 family<sup>45</sup>.

## Usage Notes

The ATAC-seq data processing pipeline, including read mapping, peak calling, IDR analysis, and read counting were run on the Linux operating system. The optimized parameters are provided in the main text. All R source codes used for the downstream data analyses and visualization are provided in Supplementary File 1.

## Code Availability

The R codes used for correlation analysis, identification of tissue-specific chromatin accessible regions, and tissue-specific TFs are available in the supplementary materials (Supplementary File 1). A repository list containing the chromatin accessibility raw count matrix and the motif enrichment matrix is available online<sup>32</sup>.

## References

1. Consortium, I. H. G. S. Initial sequencing and analysis of the human genome. *Nature* **409**, 860 (2001).
2. Venter, J. C. *et al.* The sequence of the human genome. *Science* **291**, 1304–1351 (2001).
3. Rivera, C. M. & Ren, B. Mapping human epigenomes. *Cell* **155**, 39–55 (2013).
4. Shen, Y. *et al.* A map of the cis-regulatory sequences in the mouse genome. *Nature* **488**, 116 (2012).
5. Yue, F. *et al.* A comparative encyclopedia of DNA elements in the mouse genome. *Nature* **515**, 355–364 (2014).
6. Consortium, E. P. An integrated encyclopedia of DNA elements in the human genome. *Nature* **489**, 57 (2012).
7. Kundaje, A. *et al.* Integrative analysis of 111 reference human epigenomes. *Nature* **518**, 317 (2015).
8. Stunnenberg, H. G. *et al.* The International Human Epigenome Consortium: a blueprint for scientific collaboration and discovery. *Cell* **167**, 1145–1149 (2016).
9. Xu, Q. & Xie, W. Epigenome in Early Mammalian Development: Inheritance, Reprogramming and Establishment. *Trends Cell Biol* **28.3**, 237–253 (2017).



10. Eckersley-Maslin, M. A., Alda-Catalinas, C. & Reik, W. Dynamics of the epigenetic landscape during the maternal-to-zygotic transition. *Nat. Rev. Mol. Cell Biol.* **19**, 436–450 (2018).
11. Apostolou, E. & Hochedlinger, K. Chromatin dynamics during cellular reprogramming. *Nature* **502**, 462 (2013).
12. Takahashi, K. & Yamanaka, S. A decade of transcription factor-mediated reprogramming to pluripotency. *Nat. Rev. Mol. Cell Biol.* **17**, 183 (2016).
13. Karczewski, K. J. & Snyder, M. P. Integrative omics for health and disease. *Nat. Rev. Genet.* **19**, 299 (2018).
14. Li, B., Carey, M. & Workman, J. L. The role of chromatin during transcription. *Cell* **128**, 707–719 (2007).
15. Buenrostro, J. D., Giresi, P. G., Zaba, L. C., Chang, H. Y. & Greenleaf, W. J. Transposition of native chromatin for fast and sensitive epigenomic profiling of open chromatin, DNA-binding proteins and nucleosome position. *Nat. Methods* **10**, 1213–1218 (2013).
16. Meyer, C. A. & Liu, X. S. Identifying and mitigating bias in next-generation sequencing methods for chromatin biology. *Nat. Rev. Genet.* **15**, 709 (2014).
17. Buenrostro, J. D. *et al.* Single-cell chromatin accessibility reveals principles of regulatory variation. *Nature* **523**, 486 (2015).
18. Cusanovich, D. A. *et al.* Multiplex single-cell profiling of chromatin accessibility by combinatorial cellular indexing. *Science* **348**, 910–914 (2015).
19. Mezger, A. *et al.* High-throughput chromatin accessibility profiling at single-cell resolution. *Nat. Commun.* **9**, 3647 (2018).
20. Chen, X., Natarajan, K. N. & Teichmann, S. A. A rapid and robust method for single cell chromatin accessibility profiling. *Nat. Commun.* **9**, 5345 (2018).
21. Karabacak Calviello, A., Hirsekorn, A., Wurmus, R., Yusuf, D. & Ohler, U. Reproducible inference of transcription factor footprints in ATAC-seq and DNase-seq datasets using protocol-specific bias modeling. *Genome Biol.* **20**, 42 (2019).
22. Corces, M. R. *et al.* An improved ATAC-seq protocol reduces background and enables interrogation of frozen tissues. *Nat. Methods* **14**, 959–962 (2017).
23. Dennis, D. J. *et al.* Neurog2 and Ascl1 together regulate a postmitotic derepression circuit to govern laminar fate specification in the murine neocortex. *Proc. Natl Acad. Sci.* **114**, 4934–4943 (2017).
24. Kajimura, S. *et al.* Initiation of myoblast to brown fat switch by a PRDM16–C/EBP- $\beta$  transcriptional complex. *Nature* **460**, 1154 (2009).
25. Xanthopoulos, K. G. *et al.* The different tissue transcription patterns of genes for HNF-1, C/EBP, HNF-3, and HNF-4, protein factors that govern liver-specific transcription. *Proc. Natl Acad. Sci.* **88**, 3807–3811 (1991).
26. Fickett, J. W. Quantitative discrimination of MEF2 sites. *Mol. Cell Biol.* **16**, 437–441 (1996).
27. Lu, J., McKinsey, T. A., Zhang, C.-L. & Olson, E. N. Regulation of skeletal myogenesis by association of the MEF2 transcription factor with class II histone deacetylases. *Mol. Cell* **6**, 233–244 (2000).
28. Fischer, A. W., Cannon, B. & Nedergaard, J. Optimal housing temperatures for mice to mimic the thermal environment of humans: An experimental study. *Mol. Metab* **7**, 161–170 (2018).
29. Shang, Z. *et al.* Single-cell RNA-seq reveals dynamic transcriptome profiling in human early neural differentiation. *Gigascience* **7**, 1–19 (2018).
30. Huang, J. *et al.* A reference human genome dataset of the BGISEQ-500 sequencer. *Gigascience* **6**, 1–9 (2017).
31. Koh, P. W. *et al.* An atlas of transcriptional, chromatin accessibility, and surface marker changes in human mesoderm development. *Sci. Data* **3**, 160109 (2016).
32. Liu C.-Y. *et al.* An ATAC-seq atlas of chromatin accessibility in mouse tissues. *figshare*, <https://doi.org/10.6084/m9.figshare.c.4436264.v1> (2019).
33. Zhang, Y. *et al.* Model-based analysis of ChIP-Seq (MACS). *Genome Biol.* **9**, R137 (2008).
34. Li, Q., Brown, J. B., Huang, H. & Bickel, P. J. Measuring reproducibility of high-throughput experiments. *Ann. Appl. Stat* **5**, 1752–1779 (2011).
35. Quinlan, A. R. & Hall, I. M. BEDTools: a flexible suite of utilities for comparing genomic features. *Bioinformatics* **26**, 841–842 (2010).
36. Barrera, L. O. *et al.* Genome-wide mapping and analysis of active promoters in mouse embryonic stem cells and adult organs. *Genome Res.* **18**, 46–59 (2008).
37. Schug, J. *et al.* Promoter features related to tissue specificity as measured by Shannon entropy. *Genome Biol.* **6**, R33 (2005).
38. Xie, W. *et al.* Epigenomic analysis of multilineage differentiation of human embryonic stem cells. *Cell* **153**, 1134–1148 (2013).
39. Heinz, S. *et al.* Simple combinations of lineage-determining transcription factors prime cis-regulatory elements required for macrophage and B cell identities. *Mol. Cell* **38**, 576–589 (2010).
40. CNGB Nucleotide Sequence Archive <https://db.cngb.org/cnsa/project/CNP0000198/public/> (2018).
41. NCBI Sequence Read Archive <http://identifiers.org/ncbi/insdc.sra:SRP167062> (2018).
42. ENCODE <https://www.encodeproject.org/experiments/ENCSR451NAE/> (2017).
43. ENCODE <https://www.encodeproject.org/experiments/ENCSR102NGD/> (2017).
44. Söllner, J. F. *et al.* An RNA-Seq atlas of gene expression in mouse and rat normal tissues. *Sci. Data* **4**, 170185 (2017).
45. Zhou, Q. *et al.* A mouse tissue transcription factor atlas. *Nat. Commun.* **8**, 15089 (2017).
46. Sonawane, A. R. *et al.* Understanding tissue-specific gene regulation. *Cell Rep.* **21**, 1077–1088 (2017).

## Acknowledgements

We thank all members of the Cell and Development Lab (BGI) for helpful comments and Jian Zhang and Jie Chen from Shenzhen Institutes of Advanced Technology for assistance with sample collection. This work was supported by the National Key R&D Program of China (No. 2016YFC1303902), the Shenzhen Peacock Plan (No. KQTD20150330171505310), and the Science, Technology and Innovation Commission of Shenzhen Municipality (No. JCYJ20160531194327655).

## Author Contributions

C.L., L.L., M.W. and X.W. conceived the idea. C.L. and M.W. collected samples. M.W. and C.L. generated the data. J.X., J. Xia, J.L., T.F., M.C. and Y.Y. assisted with the experiments. X.W. analyzed the data with the assistance of C.L., X.D., P.Z. and L.W.. C.L. wrote the manuscript with the input of X.W. and M.W.. L.L. and B.A.P. supervised the study and revised the manuscript. X.Z., F.C., W.Z., A.C. and Z.S. provided helpful comments on this study. All authors reviewed and approved the final manuscript.

## Additional Information

**Supplementary information** is available for this paper at <https://doi.org/10.1038/s41597-019-0071-0>.

**Competing Interests:** The authors declare no competing interests.

**Publisher's note:** Springer Nature remains neutral with regard to jurisdictional claims in published maps and institutional affiliations.



**Open Access** This article is licensed under a Creative Commons Attribution 4.0 International License, which permits use, sharing, adaptation, distribution and reproduction in any medium or format, as long as you give appropriate credit to the original author(s) and the source, provide a link to the Creative Commons license, and indicate if changes were made. The images or other third party material in this article are included in the article's Creative Commons license, unless indicated otherwise in a credit line to the material. If material is not included in the article's Creative Commons license and your intended use is not permitted by statutory regulation or exceeds the permitted use, you will need to obtain permission directly from the copyright holder. To view a copy of this license, visit <http://creativecommons.org/licenses/by/4.0/>.

The Creative Commons Public Domain Dedication waiver <http://creativecommons.org/publicdomain/zero/1.0/> applies to the metadata files associated with this article.

© The Author(s) 2019